Sea ice and its effect on CO_2 flux between the atmosphere and the Southern Ocean interior

Brice Loose[1] and Peter Schlosser[2,3,4]

Received 19 July 2010; revised 9 August 2011; accepted 30 August 2011; published 15 November 2011.

[1] The advance and retreat of sea ice produces seasonal convection and stratification, dampens surface waves and creates a separation between the ocean and atmosphere. These are all phenomena that can affect the air-sea gas transfer velocity (k_{660}), and therefore it is not straightforward to determine how sea ice cover modulates air-sea flux. In this study we use field estimates k_{660} to examine how sea ice affects the net gas flux between the ocean and atmosphere. An inventory of salinity, ^{3}He, and CFC-11 in the mixed layer is used to infer k_{660} during the drift of Ice Station Weddell in 1992. The average of k_{660} is 0.11 m d^{-1} across nearly 100% ice cover. In comparison, the only prior field estimates of k_{660} are disproportionately larger, with average values of 2.4 m d^{-1} across 90% sea ice cover, and 3.2 m d^{-1} across approximately 70% sea ice cover. We use these values to formulate two scenarios for the modulation of k_{660} by the fraction of sea ice cover in a 1-D transport model for the Southern Ocean seasonal ice zone. Results show the net CO_2 flux through sea ice cover represents 14–46% of the net annual air-sea flux, depending on the relationship between sea ice cover and k_{660}. The model also indicates that as much as 68% of net annual CO_2 flux in the sea ice zone occurs in the springtime marginal ice zone, which demonstrates the need for accurate parameterizations of gas flux and primary productivity under partially ice-covered conditions.

Citation: Loose, B., and P. Schlosser (2011), Sea ice and its effect on CO_2 flux between the atmosphere and the Southern Ocean interior, *J. Geophys. Res.*, *116*, C11019, doi:10.1029/2010JC006509.

1. Introduction

[2] The Southern Ocean south of 50°S, including its seasonal ice zone (SIZ), is thought to be among the most important oceanic regions for regulation of atmospheric CO_2 by restricting the ventilation of the deep ocean carbon reservoir and through biological export production [*Marinov et al.*, 2006]. In the modern ocean, the outgassing of biological carbon is balanced by uptake of anthropogenic carbon and determining the net transport from these two large fluxes has proven challenging. Estimates of the net air-sea CO_2 flux into the Southern Ocean have undergone progressive downward revision from approximately 0.47 Pg C yr^{-1} [*Takahashi et al.*, 2002] to 0.4 Pg C yr^{-1} [*McNeil et al.*, 2007], and most recently to 0.05 Pg C yr^{-1} [*Takahashi et al.*, 2009, hereinafter T09]. The explanation for this successive decrease in the Southern Ocean carbon sink is partly due to improved data coverage in both winter and summer within the SIZ (T09), but may also be due to stronger upwelling of old deep water that is high in natural CO_2 [*Le Quéré et al.*, 2007; *Lovenduski et al.*, 2008]. Both of these lines of evidence point to an important flux of CO_2 from the ocean to the atmosphere in austral fall and winter. At this stage, there are indications that changes in the upper ocean dynamics (e.g., upwelling and sea ice cover) are affecting the natural carbon cycle of the ocean in both the northern [*Arrigo et al.*, 2008b] and southern [*Le Quéré et al.*, 2007] hemispheres. However, all of these processes depend on the rate of air-sea gas exchange and its interaction with the sea ice cover – an interaction that is not well understood.

[3] At its maximum extent, Antarctic sea ice covers approximately 39% of the ocean surface area south of 50°S [*Meier et al.*, 2006], representing a significant physical barrier to air-sea exchange. The advance of the ice pack is asynchronous with the weakening of surface ocean stratification, producing a turbulent water column that is best conditioned for tracer transport to the ocean interior at the time when ice cover is restricting the area across which gas exchange can take place. As the sea ice pack retreats in spring, solar radiation and melting sea ice restore stratification, fostering the spring bloom, which reduces aqueous CO_2 and may enhance the air-sea concentration gradient. This combination of processes make it difficult to constrain the magnitude of air-sea CO_2 flux in the SIZ, primarily because of (1) the difficulty in estimating the strength and timing of net biological export of CO_2 from the surface ocean and (2) our incomplete understanding of gas transport across the ocean surface layer and its modulation by sea ice formation, deformation and

[1]Department of Marine Chemistry and Geochemistry, Woods Hole Oceanographic Institution, Woods Hole, Massachusetts, USA.
[2]Lamont-Doherty Earth Observatory, Earth Institute at Columbia University, Palisades, New York, USA.
[3]Departmment of Earth and Environmental Engineering, Columbia University, New York, New York, USA.
[4]Department of Earth and Environmental Sciences, Columbia University, New York, New York, USA.

0148-0227/11/2010JC006509

melt. For lack of an alternative, flux estimates have relied upon the wind speed parameterization of gas exchange developed for the open ocean to estimate the gas transfer velocity (k) [*Takahashi et al.*, 1997; *Arrigo and Van Dijken*, 2007; *McNeil et al.*, 2007], but there is little theoretical basis nor empirical evidence to support its application in the presence of sea ice. In sea ice covered regions, turbulence can be produced through buoyant convection and the promotion of current shear between the water and the ice [*McPhee*, 1992] in addition to steep short-fetch wind-generated waves, potentially increasing gas transfer velocities above what would be expected in the open ocean.

[4] Studies of CO_2 exchange in sea ice-covered regions have sought to understand the impact of both the physical and biological properties of sea ice on the surface ocean CO_2 budget. *Yager et al.* [1995] proposed a "seasonal rectification hypothesis" for the Arctic wherein respiration CO_2 remained trapped by sea ice until spring, when sea ice melt and stratification cause high primary production. This scenario leads to the expectation that sea ice-covered regions like the Arctic are a net sink for atmospheric CO_2. In the coastal Southern Ocean, *Gibson and Trull* [1999] and *Sweeney* [2003] report similar results with pCO_2 being drawn down by ice algae even before the onset of sea ice melt [*Gibson and Trull*, 1999]. *Sweeney* [2003] used $\delta^{18}O$ and salinity to constrain water mass exchange in the Ross Sea, and thereby affirmed the rectification hypothesis caused by primary production in the sea ice before and after breakup. Those authors point to the persistent O_2 deficit as an indicator that gas exchange is reduced in winter. In contrast to these observations *Bakker et al.* [1997] observed CO_2 supersaturation in the Weddell Gyre as ice cover retreated, implying a flux of CO_2 to the atmosphere, and *Jones et al.* [2010] report that both phytoplankton and alkalinity, deposited in the surface ocean during sea ice melt may result in high CO_2 uptake during summer. However, as *Yager et al.* [1995] noted, the seasonal rectification of CO_2 in the surface ocean depends upon the rate of air-sea gas exchange and upon the upwelling and diapycnal exchange into the mixed layer, which cannot be inferred from oxygen and inorganic carbon alone. *Sarmiento et al.* [1992] demonstrated that CO_2 uptake by the ocean is most sensitive to the rate of air-sea gas exchange in upwelling/downwelling regions where fast mixing in the upper ocean can transport surface properties to the interior.

[5] This study considers air-sea gas transfer through the sea ice cover in more detail by assembling estimates of k from the literature, from tracer data in the seasonal ice zone and from the assumptions used in carbon cycle estimates. These data are used to estimate the net impact of seasonal ice cover on the time-integrated uptake of transient tracers. Section 2.1 provides a brief review of the one field estimate of k in sea ice covered regions that exists in the literature. In section 2.2 we estimate air-sea gas transfer using a mass balance inversion applied to CFC-11, ^3He and salinity along the Ice Station Weddell drift track. In section 3 we explore three scenarios of the scaling relationship between the fraction of open water and k. Each scenario is applied to two gases: CFC-11 and CO_2 using a one-dimensional model of the ocean surface layer (OSL) to quantify gas transport from the atmosphere to the surface ocean beneath the pycnocline. These simple simulations act as a sensitivity experiment by probing the range of net air-sea flux produced from the different estimates of k. The results also point to the importance of constraining the effects of physical, as well as biological, exchange processes on CO_2 in the springtime marginal ice zone.

2. Gas Transfer Through Partial Ice Cover

2.1. Prior Estimates of k Within the Sea Ice Pack

[6] To date the most direct estimate of k in the presence of sea ice comes from *Fanning and Torres* [1991], who used the ^{222}Rn deficit method in the Barents Sea to measure the gas transfer velocity during late winter 1986 and late summer 1988. In what the authors reported as greater than 90% sea ice cover, they observed ratios of ^{222}Rn to ^{226}Ra activity as high as 0.93, and a range of k_{660} (gas transfer velocity normalized to Schmidt number of 660) of 1.44 to 3.36 m d^{-1} in late winter under almost complete ice cover and k_{660} of 2.16 to 6.24 m d^{-1} during what was described as "less than 70%" ice cover. While very little information on sea ice cover and sea ice type during the late winter period is documented in the study of *Fanning and Torres* [1991], the approximately 90% ice cover condition is consistent with a survey of Advanced Very High Resolution Radiometer (AVHRR) images from 1989, which indicates that the sea ice cover was approximately 92% in the marginal seas of the Arctic, including the Barents Sea [*Lindsay and Rothrock*, 1995].

2.2. Estimate of k From a Trace Gas Mass Balance (Ice Station Weddell)

[7] During the Ice Station Weddell project (ISW) (February–June 1992) water samples were collected from the surface layer beneath the sea ice during a 5 month period [*Huber et al.*, 1994]. Water column hydrography including temperature and salinity was measured along two sections: the ISW drift track and a track occupied during the recovery cruise by the R/V NB Palmer. Simultaneous sampling for both CFC-11 and ^3He occurred for a period of approximately 29 d in April and May. The time evolution of the drifting sea ice pack can be seen in Figure 1. In this section we are looking for evidence of the gas transfer velocity through sea ice by evaluating the time evolution of multiple tracers in the mixed layer during the experiment.

[8] The track of the ice camp follows a trajectory similar to that of the Weddell Gyre, moving northward along the Antarctic Peninsula. In total, the ISW camp drifted nearly 420 km during 95 d (4.4 km d^{-1}; Figure 1). If we assume that the upper water column moved with the sea ice (same trajectory; same velocity), then changes to the sea ice-covered mixed layer will result from vertical exchange at the air-sea interface, or at the base of the mixed layer and we can formulate a tracer mass balance based on vertical fluxes. During the ISW experiment *McPhee and Martinson* [1994] observed an Ekman spiral, so this assumption is not perfect. However, the magnitude of the velocities associated with this shear is much smaller than the mean drift.

[9] The Weddell Sea mixed layer overlays Circumpolar Deep Water (CDW). The core of CDW in the Weddell Sea is found between 500 and 750 m along the ISW section, highlighted by temperatures greater than 0.6°C, and δ^3He values in excess of 8% (Figure 2). The water column properties above 500 m depth from 1 March (day 60) to 30 May

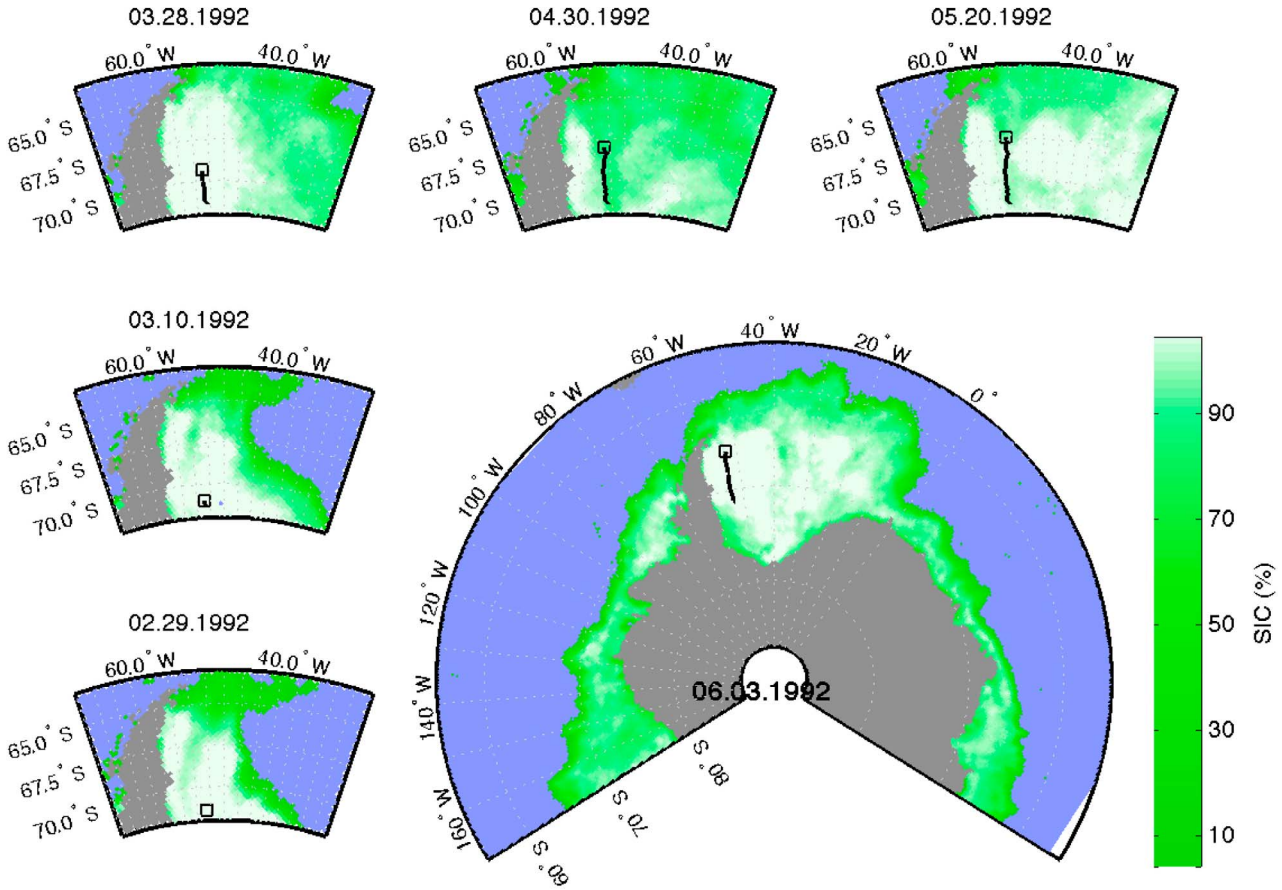

Figure 1. The time evolution of ice cover from the scanning multichannel microwave radiometer and Special Sensor Microwave Imager (SSM/I) 25 km resolution sea ice concentration during Ice Station Weddell [*Meier et al.*, 2006].

(day 150) are displayed in Figure 2, together with the depth of the 27.74 isopycnal. The inventories and average concentrations of CFC-11 and ^{3}He between the 27.74 isopycnal and the water surface are plotted in Figure 3. The inventories of these tracers track the changes in the 27.74 isopycnal, which shoals to 104 m on day 145 and deepens to 185 m by day 150 (Figure 2). The vertically averaged δ_{3He} values follow a similar trend as the ^{3}He inventory, but the average CFC-11 concentrations are less variable, increasing gradually throughout the period. Overall, the CFC-11 inventory increased by approximately 2.2×10^5 pmol m^{-2} between days 128 and 149.

[10] The change in these inventories can be used to calculate the vertical fluxes, i.e., entrainment of CDW and gas exchange, into and out of the mixed layer that is bounded by the air-sea interface and the 27.74 isopycnal. The tracer balance can be written as follows:

$$\frac{1}{\rho}\frac{dM}{dt} = k\left(C_{ATM} - \overline{C^t}\right) + C_{CDW}F_{CDW} + \overline{C^t}\Delta_{ML} \qquad (1)$$

where M represents the mass of tracer in a well-mixed volume bounded between the partially ice-covered water surface and an isopycnal. C_{CDW}, $\overline{C^t}$, and C_{ATM} represent the tracer concentrations (mol kg^{-1}) in CDW, in the bounded volume at time t, and in equilibrium with the atmosphere, respectively. $\overline{C^t}$ is determined as the vertical average of values between the isopycnal surface and the water surface taken from the time of the hydrographic cast. F_{CDW} is the entrainment/detrainment rate in m d^{-1} into or out of the isopycnal volume as a result of addition/subtraction of CDW, k is the gas transfer velocity (m d^{-1}) and ρ is the density of seawater. The term Δ_{ML} represents spatial changes in the mixed layer depth that arise as a consequence of interaction with topography or other stationary modifications to the mixed layer. This formulation assumes a negligible effect on the tracer budgets from freezing or melting of sea ice.

[11] If we consider prior estimates of F_{CDW} and k as well as ice growth, we can evaluate the scale of each term on the right hand side of equation (1). In the Weddell Sea, the entrainment of CDW, based on ^{3}He measurements is 0.28–0.39 m d^{-1} [*Hohmann et al.*, 2003]. If gas transfer scales with ice cover, as assumed by T09, k_{660} would be ~0.36 m d^{-1} under conditions of approximately 10% open water (f = 0.1). Finally, sea ice growth or melt can result in a change in salinity, gas content and density of the isopycnal inventory. However, very rapid sea ice growth would be 0.02 m d^{-1} [*Cox and Weeks*, 1983], an order of magnitude less than either entrainment or gas exchange, so we have neglected the effect of sea ice in this analysis. The similarity in magnitude between F_{CDW} and k indicates that the effect of gas transfer should be detectable in this mass balance formulation.

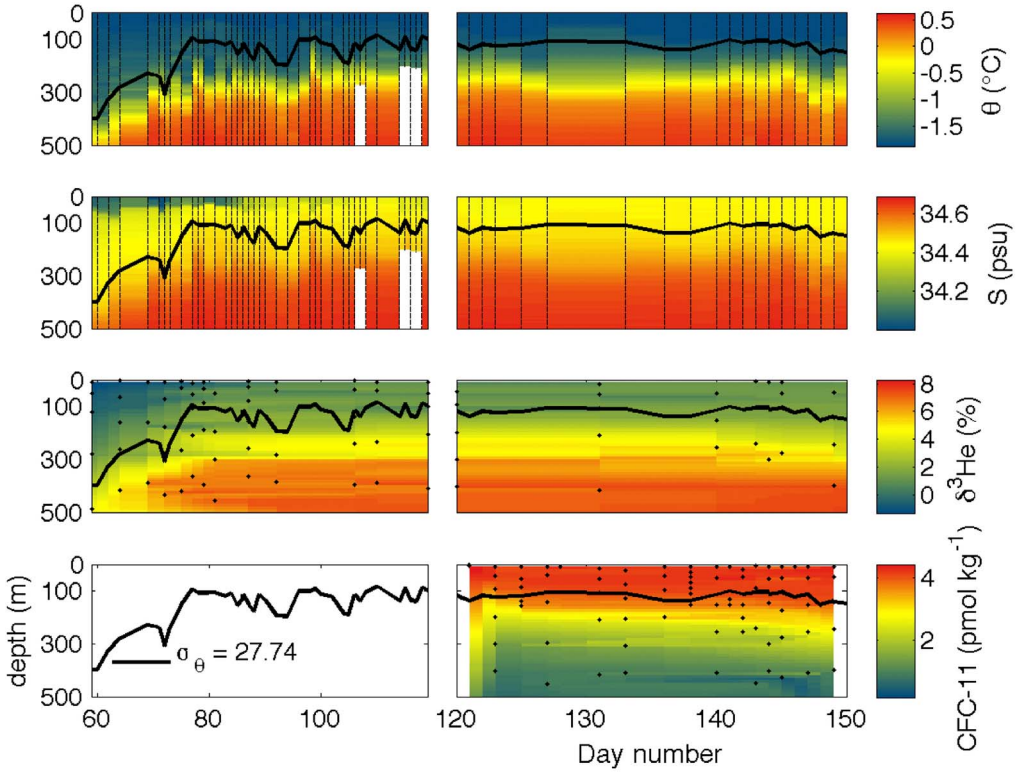

Figure 2. The time evolution of potential temperature, θ, salinity, S, δ^3He, and CFC-11 along the Ice Station Weddell (ISW) drift track from 1 March to 30 May 1992. The solid line indicates the location of the σ_θ = 27.74 isopycnal.

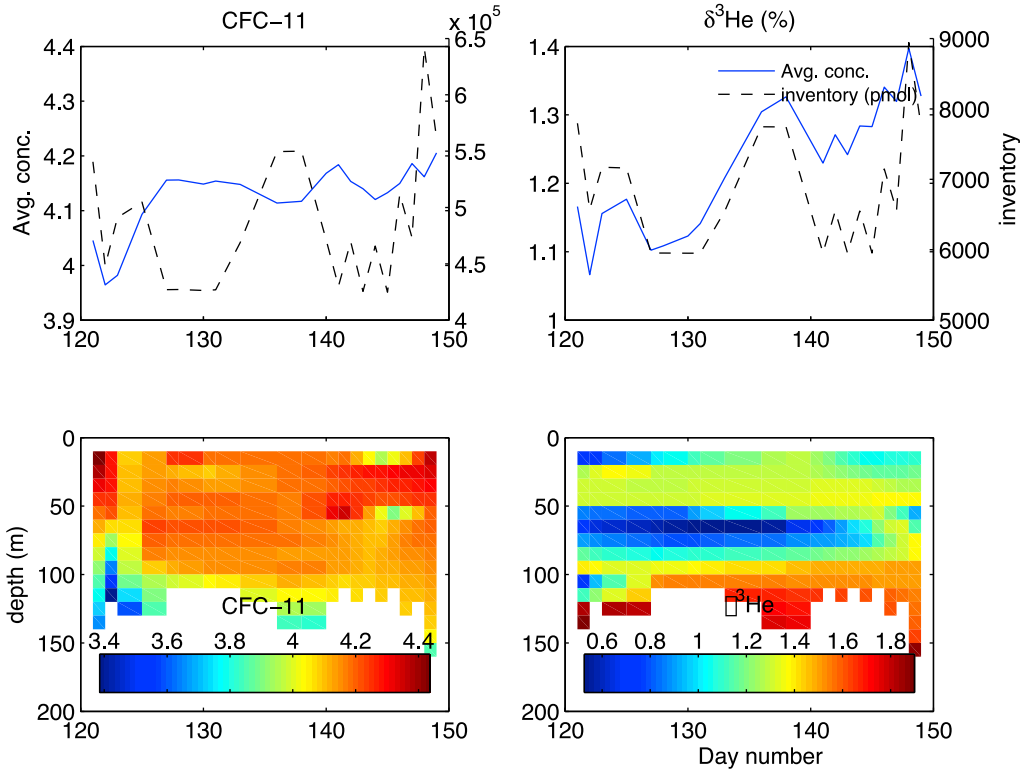

Figure 3. (top) The inventory and average concentration of CFC-11 and δ^3He above the 27.74 isopycnal and (bottom) the gridded distribution of CFC-11 and δ^3He along the ISW drift track from day 120 to day 150.

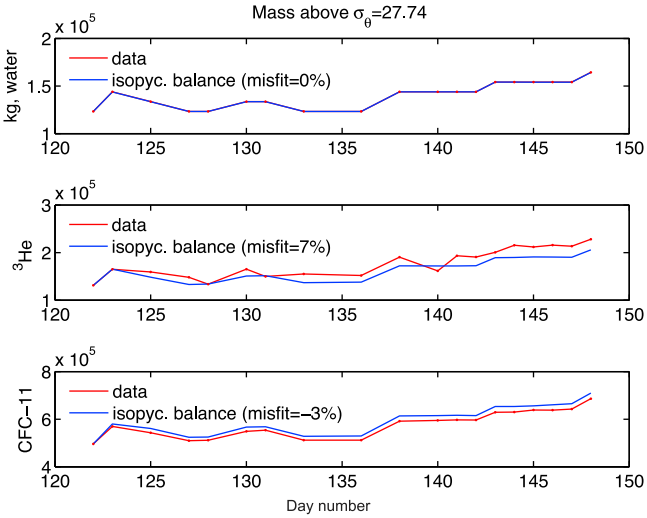

Figure 4. The mass inventory of water, ^{3}He, and CFC-11 between the 27.74 isopycnal and the water surface, based on the ISW data and based on the $\underline{\underline{C}} \cdot \underline{x}$ inventory reconstruction.

[12] As an additional constraint to the tracer mass balance, the mass balance for water above the reference isopycnal is included as

$$\frac{1}{\rho}\frac{dM}{dt} = F_{CDW} + \Delta_{ML}. \tag{2}$$

This formulation does not consider the effect of surface heat loss on the isopycnal volume, but surface heat loss is small in comparison to the water mass fluxes associated with entrainment, which can be demonstrated by expanding the left side of equation (2),

$$\frac{dM}{dt} = \rho\frac{dV}{dt} + V\frac{d\rho}{dt}, \tag{3}$$

where the surface heat loss affects the term, $d\rho/dt$. Based on the linearized equation of state for density $\rho = \rho_0[1 - \alpha(T - T_0)]$, and an estimate of 5 W m^{-2} of radiative heat loss through sea ice cover [*Lytle and Ackley*, 1996], the change in density from radiative heat loss can be estimated as,

$$V\frac{d\rho}{dt} = \frac{d\rho}{dT}\frac{dT}{dt} = -\rho_0\alpha\frac{\dot{Q}}{\rho_0 Cp} = \mathrm{O}(10^{-1})\text{kg m}^{-2}\text{ d}^{-1}, \tag{4}$$

where α is the thermal expansion coefficient ($\alpha = 1.6 \times 10^{-4}$ K^{-1}), and C_p is the specific heat capacity of water. In comparison, entrainment and sea ice formation $\rho dV/dt$, constitute O(10^2) kg m^{-2} d^{-1}, as shown above.

[13] Equation (1) can be written separately for CFC-11 and ^{3}He. To account for the changing isopycnal volume, the left side of equation (1) must be expanded to

$$\frac{V^t}{\Delta t}\left(\overline{C^{t+1}} - \overline{C^t}\right) + \frac{\overline{C^t}}{\Delta t}\left(M_W^{t+1} - M_W^t\right) = \rho C_{CDW} F_{CDW} + k_{660}\rho\left(\frac{Sc_C}{660}\right)^{-0.5}\left(C_{ATM} - \overline{C^t}\right) + \rho\overline{C^t}\Delta_{ML}. \tag{5}$$

[14] The same equation applies to the salt balance if the gas exchange term is removed and evaporation neglected. These three equations together with equation (2) for water mass conservation represent a four equation system for three unknowns (F_{CDW}, k and Δ_{ML}) and the discrete version of these linear equations can be written as follows:

$$\underline{\underline{C}} \cdot \underline{x} = \underline{d}$$

$$\begin{bmatrix} \rho C_{CDW} & \rho\overline{C^t} & \rho\left(\frac{Sc_{CFC-11}}{660}\right)^{-0.5}\left(C_{ATM} - \overline{C^t}\right) \\ \rho He_{CDW} & \rho\overline{He^t} & \rho\left(\frac{Sc_{He}}{660}\right)^{-0.5}\left(He_{ATM} - \overline{He^t}\right) \\ \rho S_{CDW} & \rho\overline{S^t} & 0 \\ \rho & \rho & 0 \end{bmatrix} \bullet \begin{bmatrix} F_{CDW} \\ \Delta_{ML} \\ k_{660} \end{bmatrix} = \begin{bmatrix} \frac{M_W^t}{\Delta t}\left(\overline{C^{t+1}} - \overline{C^t}\right) + \frac{\overline{C^t}}{\Delta t}\left(M_W^{t+1} - M_W^t\right) \\ \frac{M_W^t}{\Delta t}\left(\overline{He^{t+1}} - \overline{He^t}\right) + \frac{\overline{He^t}}{\Delta t}\left(M_W^{t+1} - M_W^t\right) \\ \frac{M_W^t}{\Delta t}\left(\overline{S^{t+1}} - \overline{S^t}\right) + \frac{\overline{S^t}}{\Delta t}\left(M_W^{t+1} - M_W^t\right) \\ \frac{1}{\Delta t}\left(M_W^{t+1} - M_W^t\right) \end{bmatrix}. \tag{6}$$

C represents the CFC-11 concentration, He represents δ^3He, and S represents salinity. Equation (6) is solved by a least squares procedure when both helium and CFC-11 data are available. When either CFC-11 or ^{3}He data are missing the system can be solved with an exactly determined solution. In this case the model data difference cannot be minimized [*Tarantola*, 2005]. Equation (6) was solved using a bootstrap approach with 1500 iterations, taking a random sample of the water column values used to compute $\overline{C^t}$. This approach is a robust means to assess the variability introduced by under-sampling the population of water column values, and is used to present the results with a confidence interval of 95%.

[15] The mean concentrations of CFC-11, δ^3He and salinity beneath the 27.74 isopycnal and above 500 m (Figure 2) are 1.23 pmol kg^{-1}, 6.32% and 34.62 psu, respectively. These values are used to define C_{CDW}, He_{CDW} and S_{CDW}, i.e., the properties of water that is entrained into the 27.74 isopycnal along the drift track of ISW. Equation (6) is solved to find F_{CDW}, k and Δ_{ML} for each day from days 122 to 148. To judge the quality of the model data fit, the values in $\underline{d}$ are reconstructed from $\underline{\underline{C}} \cdot \underline{x}$, and the misfit between the mass balance and the data is defined as

$$\text{misfit} = (\underline{d}_{mb} - \underline{d}) \times 100. \tag{7}$$

[16] Both $\underline{d}_{mb}$ and $\underline{d}$ are plotted in Figure 4. The misfit is greatest for δ^3He, with a mean value of 7%, indicating that ^{3}He is least well reconstructed within the mixed layer volume. CFC-11 has a mean misfit of −3% and the misfit for water conservation is less than 1%, indicating a good overall capability of the model to reproduce the observations.

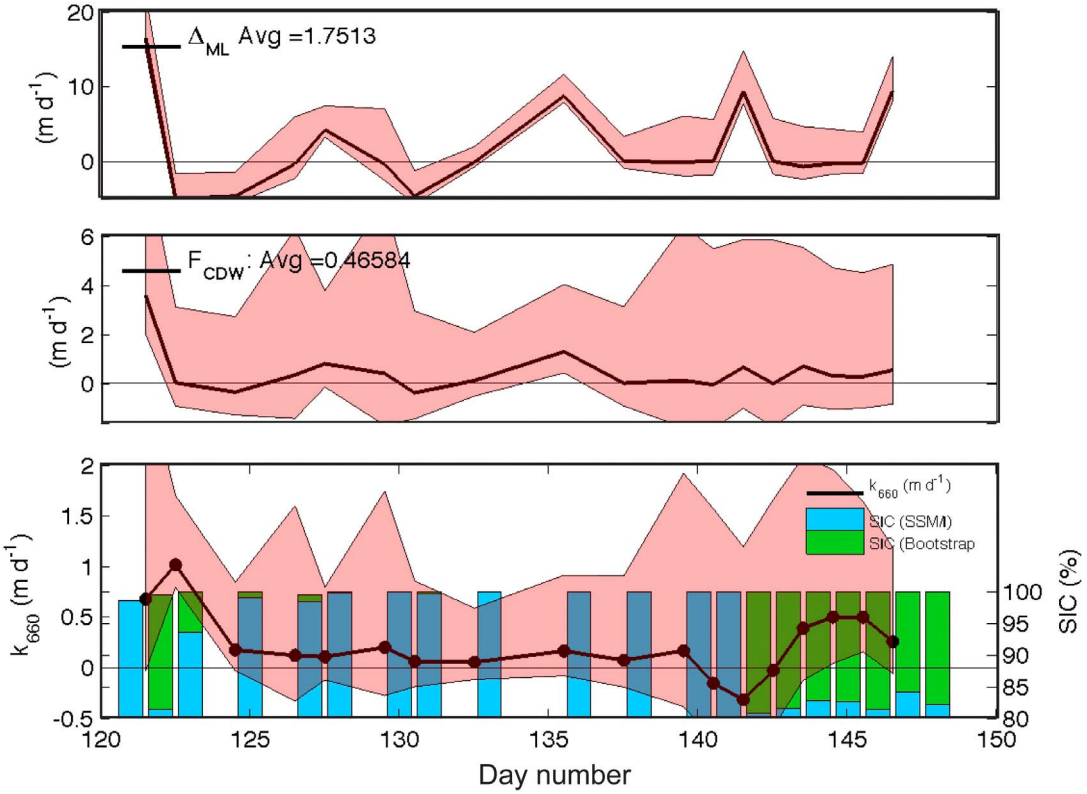

Figure 5. Results from the isopycnal mass balance, along the ISW drift track from day 122 to 147. F_{CDW}, k_{660} and Δ_{ML} are all in m d^{-1}. The bars in the third panel are the sea ice cover (SIC) in % interpolated to the location of the ISW drift track. The blue bars are estimates of SIC from the SSM/I 25 km ice cover data product, and the green bars are the NIMBUS 7 and SSM/I using the AMSR-E bootstrap algorithm [*Comiso*, 2007].

[17] The rate of entrainment of CDW into the mixed layer (F_{CDW}) varies between −0.4 and 1.3 m d^{-1} throughout the period with the exception of day 122 when F_{CDW} achieved its largest value of 3.6 m d^{-1} (Figure 5). The average of F_{CDW} is 0.47 m d^{-1} from day 122 to 148. In general, the pattern of F_{CDW} is opposite to the trend in the 27.74 isopycnal (Figure 2); for example, shoaling of σ_θ = 27.74 on day 122 is accompanied by a negative value for F_{CDW}. The mean of F_{CDW} (0.47 m d^{-1}) is close to the range of 0.28–0.39 m d^{-1} estimated by *Hohmann et al.* [2003] from the sea ice–covered central Weddell Sea in 1994.

[18] The behavior of Δ_{ML} is similar to that of F_{CDW} but it reflects expansions and contractions of the mixed layer that are not accompanied by a change in the mean properties of S, δ^3He and CFC-11. When the mixed-layer shoals (e.g., on day 122), Δ_{ML} becomes negative reflecting the decrease in depth. Overall, Δ_{ML} varies between −5 and 16 m d^{-1} with an average value of 1.8 m d^{-1}. If we observe the time evolution of the 27.74 isopycnal it is apparent that the volume changes between this isopycnal and the water surface are larger than would be expected from vertical processes alone and likely represent intrinsic horizontal variability in the water column, such as interactions with bathymetry or flow convergence/divergence on a larger scale. One example of such heterogeneity is the Taylor column above the Maud Rise described by *Ou* [1991], but flow convergence associated with the Weddell Gyre, eddies and submesoscale processes could all potentially affect Δ_{ML}. The net result of the inversion is a picture in which a net flow convergence (manifested as positive Δ_{ML} ~1.8 m d^{-1}) and a smaller entrainment flux of CDW (0.47 m d^{-1}) drive a net influx of CFC-11 and efflux of ^{3}He to move toward equilibrium.

[19] The mean value for k_{660} between days 122 and 147 is 0.22 ± 0.31 (N = 18) m d^{-1}, including two values on days 141 and 142 that are negative. The term k is positive by definition so a negative result in the solution to equation (6) indicates an unrealistic solution. Equation (6) does not have a nonnegative constraint because it is physically possible for both Δ_{ML} and F_{CDW} to achieve negative values and a nonnegative constraint would therefore be unrealistic. To discern the error envelope, the 95% confidence interval has been computed for each estimate of k (depicted as shaded area in Figure 5). The confidence interval spans the value of zero on the *y* axis indicating that all but three of the estimates of k are not unique from zero. The uniquely nonzero values of k from equation (6) are 1.01, 0.49 and 0.47 m d^{-1}. If we recalculate the average of k from day 122 to 147, substituting zero for the values that were not unique from zero, the mean of k decreases to 0.11 m d^{-1}.

[20] To determine the sea ice cover along the ISW drift track we interpolated two data products from the National Snow and Ice Data Center: the Special Sensor Microwave Imager (SSM/I) 25 km resolution satellite-based sea ice

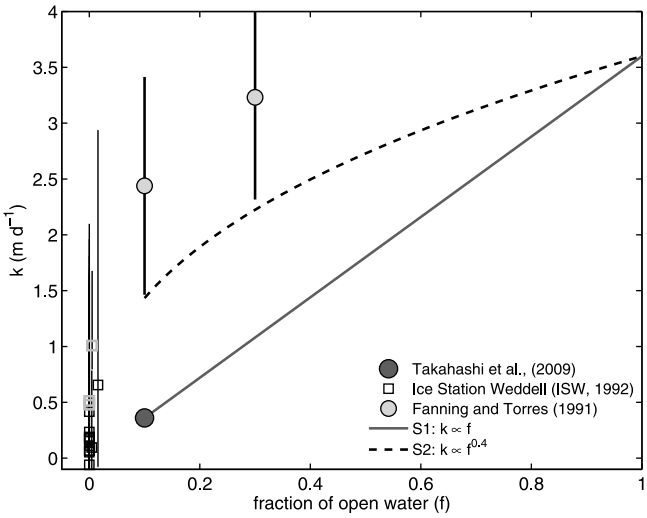

Figure 6. The relationship between gas transfer velocity (k) and the fraction of open water (f). These data represent the available measurements for air-sea gas transfer through partial ice cover. The open squares are the values from ISW that are unique from zero with 95% confidence. The values from *Fanning and Torres* [1991] reported here are averages of all values reported in their Table 1 for "Late Winter" and "Late Summer," normalized to a Schmidt number of 660.

cover [*Cavalieri et al.*, 1996], and the NIMBUS 7 and SSM/I sea ice cover using the AMSR-E bootstrap algorithm [*Comiso*, 2007]. We refer to the first as "SSM/I" and the second as the "Bootstrap." Both products show greater than 95% ice cover with the exception of day 123 and days 142 to 147. The SSM/I product shows a step change in sea ice cover occurs after day 141 when sea ice decreases from near 100% to 81% (Figure 5), while the Bootstrap product shows that the ice cover remains at nearly 100%. Reports from a participant in the ISW field program indicate that ice cover was nearly 100% for all of May when these data were collected (S. Ackley, personal communication, 2010), and there is some evidence that the Bootstrap algorithm is more accurate in its estimates of ice cover [*Steffen and Schweiger*, 1991; *Knuth and Ackley*, 2006]. On the basis of this information, we have related the estimates of k to the sea ice cover estimates from the Bootstrap algorithm.

[21] It is apparent that the average gas transfer velocity (k) with 95% confidence (0.11 m d^{-1}) is low compared to global averages of k. However, it is interesting to consider that these estimates from the Ice Station Weddell data indicate a nonzero gas exchange rate in spite of the presence of nearly 100% sea ice cover. Despite the appearance of complete sea ice cover, the kinematics of sea ice demonstrate that even when sea ice cover is near 100%, convergent and divergent motions [*Geiger and Drinkwater*, 2005] cause some fraction of the pack to remain open to the atmosphere. Some estimates put this value at 10% for the entire sea ice pack, which happens to coincide with the disagreement between satellite and image analysis [*Knuth and Ackley*, 2006], although satellite estimates do not show a consistent bias toward overestimating the sea ice cover. The estimates of k that have been produced here indicate that air-sea gas exchange does not cease, even at nearly 100% sea ice cover and this is likely a reflection of the percentage of ephemeral open water that remains.

2.3. What Can Be Said About the Tendency Between k and the Fraction of Ice Cover?

[22] We have two independent estimates of k derived from field measurements of gas tracers: those by *Fanning and Torres* [1991] from the Arctic and the estimates described above from Ice Station Weddell in the Southern Ocean. Gas transfer velocity from ISW is of little practical utility in helping to determine a scaling relationship for the sea ice zone as it relates to the limiting condition of 100% ice cover. This result is unfortunate because tracer data from ISW appears to be the only data set of inert gas tracers beneath ice cover that is suitable for an estimate of gas exchange, but it serves to emphasize the conclusion that gas exchange in sea ice covered waters remains largely unconstrained by data.

[23] If we consider the estimates of k from *Fanning and Torres* [1991] as a function of the open water fraction (f) and the hypotheses that are commonly made in carbon cycle studies, they depict two very different relationships between k and f (Figure 6). The estimates of k from *Fanning and Torres* [1991] depict a range that is 4–8 times as large as the linear scaling used by T09 under the same conditions of f (e.g., f = 0.1 – 0.3). The experiments of *Loose et al.* [2009] also indicate that gas transfer may not scale linearly with the fraction of open water, namely because the turbulence dissipation beneath the sea ice is not necessarily a strict function of fetch. These disparate estimates of k are difficult to compare, because of the difficulty in constraining the other forcing factors, namely fetch, wind speed and aqueous turbulence. In the absence of a well-established relationship we can explore different scenarios for the relationship between the gas transfer velocity and the fraction of sea ice cover in order to study the sensitivity of the net gas flux to the choice of parameterization. This is the focus of section 3.

3. Scenarios for Seasonal and Annual Gas Transport in an Ocean Surface Layer Model

[24] To evaluate the effect of sea ice on gas exchange we compare three different scenarios for modulation of k by sea ice cover: LIN: $k \propto f$: In this scenario, the fraction of sea ice cover, (1 − f), varies seasonally with a maximum of 1 − f = 0.9, a minimum of 1 − f = 0 and a period of 365 d. During maximum sea ice cover k is 10% of k in the open ocean (k_{oo}). The linear proportionality between k and f and the minimum of f = 0.1 were chosen because they are the criteria that T09 use in their most recent climatology. NLIN: Given the same seasonal cycle in f as in the LIN scenario, we assume $k \propto f^{0.4}$ as a representation of the results of *Fanning and Torres* [1991] and to reflect the experimental results of *Loose et al.* [2009] (Figure 6). This proportionality, implies that when f reaches its minimum value of 0.1, $k = 0.39\ k_{oo}$. NOICE, the third scenario, serves as a control scenario with no sea ice cover and a constant gas transfer velocity k, so that the effect of the mixed layer alone can be observed.

[25] These scenarios are applied to an inert gas, CFC-11, and a biogenic gas, CO_2. These gases have different equilibration

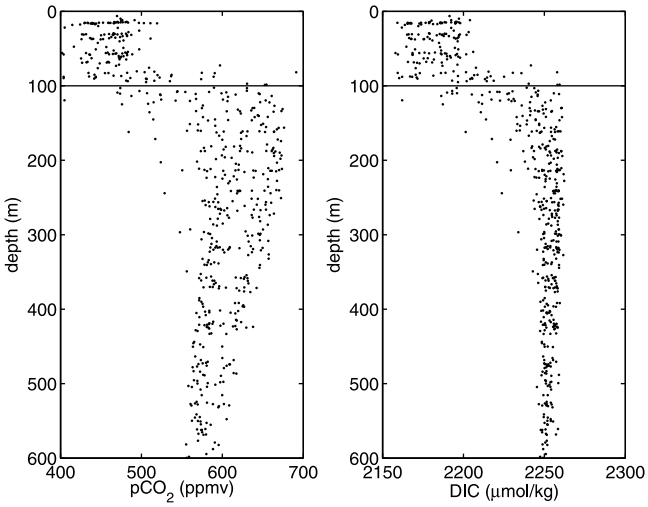

Figure 7. The 1996 S04I World Ocean Circulation Experiment (WOCE) hydrographic line, along the Antarctic coast from 80 to 120°E, south of 60°S, from early May to early July, during conditions of advancing sea ice cover. (Data available at WOCE Hydrographic Program Office, http://whpo.ucsd.edu/.)

time scales at the air-sea interface. We adopt a simplified perspective derived from the water column properties that characterize the Southern Ocean seasonal ice zone (Figure 7). The Southern Ocean SIZ consists of a mixed layer with a depth of approximately 100 m during winter, situated above the relatively warm (0.5 to 1°C) CDW that is high in dissolved inorganic carbon (DIC) and low in CFC-11. Figure 7 contains selected vertical profiles of DIC and pCO_2 along the WOCE S4I line from May and June 1996 under conditions of increasing sea ice cover.

[26] The net seasonal and interannual flux of gas that moves through the ocean surface layer (OSL) is calculated using the one-dimensional turbulent diffusion equation to simulate the serial barriers to exchange at the air-sea interface and in the mixed layer. The OSL has been formulated as a 200 m thick water column overlaying an infinite reservoir of CDW. From above, the mixed layer is seasonally covered by sea ice, and this process is represented as a reduction in the magnitude of k, proportional to the surface area of the sea ice cover. Within the OSL, the thermocline ascends and descends seasonally, one-half year out of phase with the advance of sea ice. In summer, the thermocline is located 10 m below the sea ice-free ocean surface, and in winter the thermocline increases to 100 m depth. The seasonal cycle of mixed layer convection and stratification is reproduced by varying the turbulent diffusion coefficient, $D = D(z,t)$. For each scenario, LIN, NLIN and NOICE, the seasonal cycle in D is the same.

[27] The seasonal cycles in k and D are used to condition the diffusion equation,

$$\frac{\partial C}{\partial t} - \frac{\partial}{\partial z}\left(D(z,t)\frac{\partial C}{\partial z}\right) = \sum F \tag{8}$$

subject to the Robin boundary condition on gas transfer at the air-sea interface [*Haine*, 2006],

$$z = 0: \quad C(0,t) - \frac{D}{k}\frac{\partial C}{\partial z}\bigg|_{z=0} = C_{atm} \tag{9}$$

and to a constant gas concentration at the lower boundary, within the underlying CDW plume,

$$z = H: \quad C(H,t) = C_{CDW} \tag{10}$$

[28] The Robin boundary condition is a weighted combination of the Dirichlet and Neumann boundary conditions. Here, k is gas transfer velocity, χ_{atm} is the atmospheric gas partial pressure, H is solubility coefficient and D is the turbulent diffusion coefficient. The relationship in (9) depicts the balance between disequilibrium across the air-sea interface represented by k and diffusion of gas from the interface into the far field ocean or $D\partial C/\partial z$. As k increases, $D/k \rightarrow 0$ and the surface aqueous gas concentration is moving toward equilibrium with the atmospheric concentration,

$$C(0,t) \rightarrow H\chi_{atm} \tag{11}$$

Fundamentally, the ratio of D/k depicts the competition between equilibration at the air-sea interface, and rapid mixing or subduction in a turbulent mixed layer.

[29] To compute the gas flux (F_g) across the air-sea interface, we use the mass balance by accounting for the time variation in the tracer inventory within the OSL model and add to that a first-order estimate of diffusive flux across the bottom boundary at 200 m:

$$F_g = -\frac{\Delta z}{\Delta t}\sum_{i=1}^{N}\left(C_i^{t+1} - C_i^t\right) + D\frac{\Delta C}{\Delta z}\bigg|_{i=N} \tag{12}$$

N is the number of elements in the discrete model grid. Here, the standard convention is adopted, wherein a flux from the atmosphere to the ocean is a sink, with a negative sign attached.

[30] This system is solved using an implicit finite difference solution at 100 levels with a harmonic averaging method [*Shashkov and Steinberg*, 1996] to regularize the effect of time and space-varying permittivity. A cartoon of the model domain is presented in Figure 8. Within the mixed layer, the turbulent diffusion coefficient for passive tracers is 0.2 $m^2\ s^{-1}$ (1730 $m^2\ d^{-1}$); this value originates from measurements of turbulence beneath the sea ice cover by *McPhee and Martinson* [1994] who observed that eddy thermal diffusivity approached the value of eddy viscosity, with a typical range of 0.15 to 0.25 $m^2\ s^{-1}$. Beneath the mixed layer, the diapycnal diffusivity decreases by three orders of magnitude to 0.5×10^{-4} $m^2\ s^{-1}$ (4.3 $m^2\ d^{-1}$) [*Schlosser et al.*, 1987]. The average value of k_{oo} of CO_2 for the seasonal ice zone is 3.6 m d^{-1} (T09). Figure 9 shows the time variation in k_{oo} for LIN, NLIN and NOICE as well as the vertical and temporal variation in D. The OSL, as a one-dimensional model, does not consider processes that vary laterally such as katabatic winds, flow heterogeneities, bathymetric effects and spatial variations in ice thickness.

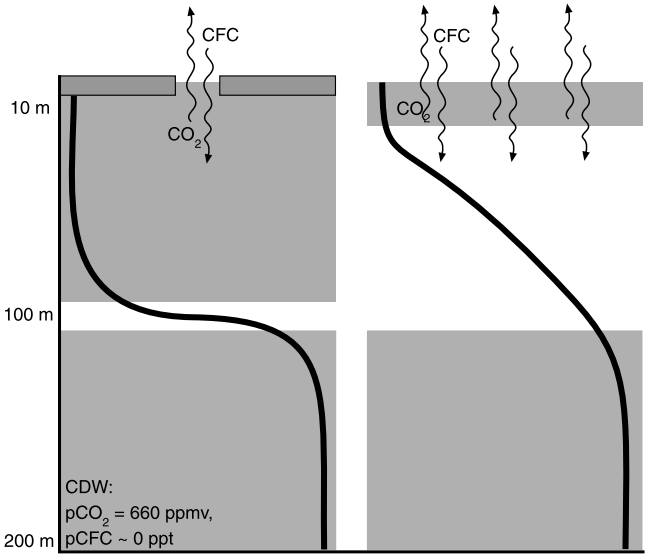

Figure 8. Cartoon of the ocean surface layer model for the Southern Ocean, used to monitor the uptake of CFC-11 and ventilation of CO_2.

3.1. CFC-11 Transport Through the OSL

[31] The simulations for CFC-11 were carried out using the atmospheric time history for the southern hemisphere from 1945 until 1995 [*Walker et al.*, 2000] to establish χ_{atm} in equation (11). The *Sc* corrected value of k_{oo} for CFC-11 at 0°C is $k_{CFC\text{-}11} = 2.7$ m d^{-1}. The annual average of $k_{CFC\text{-}11}$ from the periodic forcing conditions for LIN, NLIN and NOICE are 1.3, 1.7 and 2.7 m d^{-1}, respectively (Table 1).

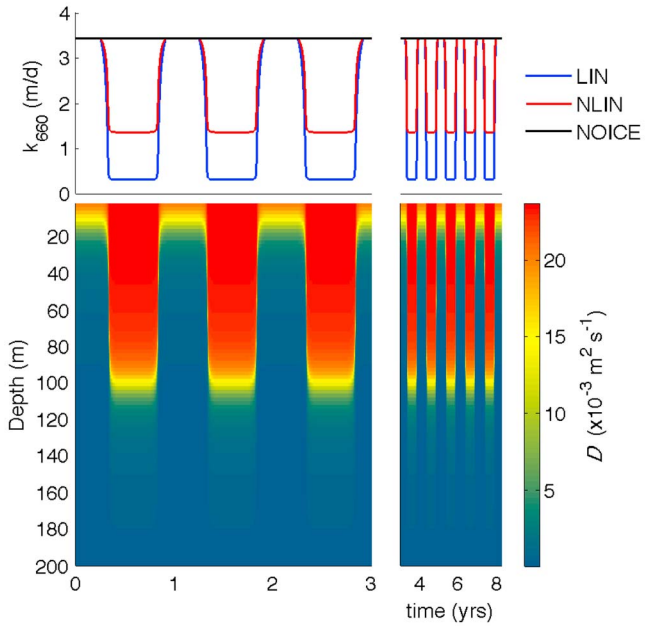

Figure 9. The seasonal forcing conditions applied to the ocean surface layer model. Scenario LIN, NLIN, and NOICE represent three unique seasonal cycles in the modulation of *k* by sea ice cover; the seasonal cycle in turbulent diffusion, D, is the same in all three scenarios.

Table 1. Forcing Parameters for the Ocean Surface Layer Simulation Described in Section 3[a]

	LIN	NLIN	NOICE
D (ice free), m^2 h^{-1}	2.6	2.6	2.6
D (ice covered), m^2 h^{-1}	66.4	66.4	66.4
L (ice-free), m	10	10	10
L (ice covered), m	100	100	100
$k_{CFC\text{-}11}$ (ice free), m d^{-1} (^{1}cm h^{-1})	2.7 (11.1)	2.7 (11.1)	2.7 (11.1)
$k_{CFC\text{-}11}$ (ice covered), m d^{-1} (^{1}cm h^{-1})	0.3 (1.1)	0.9 (3.7)	2.7 (11.1)
$k_{CFC\text{-}11}$ (annual average), m d^{-1} (^{1}cm h^{-1})	1.3 (5.6)	1.7 (7.1)	2.7 (11.1)
k_{CO2} (ice free), m d^{-1} (^{1}cm h^{-1})	3.4 (14.3)	3.4 (14.3)	3.4 (14.3)
k_{CO2} (ice covered), m d^{-1} (cm h^{-1})	0.3 (1.3)	(4.5) 1.1	3.4 (14.3)
k_{CO2} (annual average), m d^{-1} (cm h^{-1})	1.7 (7.2)	2.2 (9.1)	3.4 (14.3)
Net flux (mol-C m^{-2} yr^{-1})	2.3	2.8	3.9

[a]The values for *D* in the ocean surface layer model represent the harmonic average from the top 100 m of the water column.

[32] Because of the transient nature of the CFC concentration in the atmosphere, the model does not reach an oscillatory steady state. Nonetheless, it is possible to note several interesting differences in the uptake rates for LIN, NLIN and NOICE. Figures 10a and 10c presents a 2 year interval of the 60 year simulation during which the atmospheric CFC-11 concentration increases nearly linearly. The solid black line represents the surface aqueous CFC-11 concentration, calculated for solubility equilibrium (in parts per trillion; pptv) for 100% open water (NOICE), and the red and blue lines indicate pCFC-11 for seasonal sea ice cover with a minimum open water fraction f of 0.1, resulting in $k = 0.1\ k_{oo}$ (LIN) and $k = 0.39\ k_{oo}$ (NLIN), respectively. The seasonality in the surface ocean concentration is readily apparent in all three scenarios. However, the surface concentration decreases most strongly in the presence of sea ice (LIN and NLIN). Throughout the year, the surface ocean concentration remains undersaturated by at least 10%, even in scenario NOICE (no sea ice cover). As the mixed layer deepens in fall and winter, the CFC-11 saturation at the surface decreases in the presence of sea ice cover for the NLIN and LIN scenarios to 69% and 55%, respectively. During this period, the surface ocean mixes rapidly and is least resistant to CFC-11 uptake, as evidenced by the strong increase in flux that takes place in scenario NOICE (Figure 10c negative sign indicates atmosphere-to-ocean flux). During austral fall and winter the presence of sea ice cover in scenarios LIN and NLIN decreases the gas flux as compared to scenario NOICE. The fluxes in scenarios LIN and NLIN increase throughout the winter because of the increasing air-sea CFC gradient, as more low-CFC CDW is entrained into the mixed layer, diluting the surface ocean concentration.

[33] Despite the reduction in air-sea exchange due to the presence of sea ice, the flux through the sea ice covered surface represents 24% of the total annual CFC-11 flux for scenario LIN and 58% of the total annual CFC-11 flux for scenario NLIN (Figure 10d). However, it is interesting to note that at the end of winter, much of the difference between scenarios LIN, NLIN and NOICE is eroded when the melting sea ice cover exposes a significantly depleted surface layer to the atmosphere in scenarios LIN and NLIN. The retreat of the sea ice cover causes an immediate

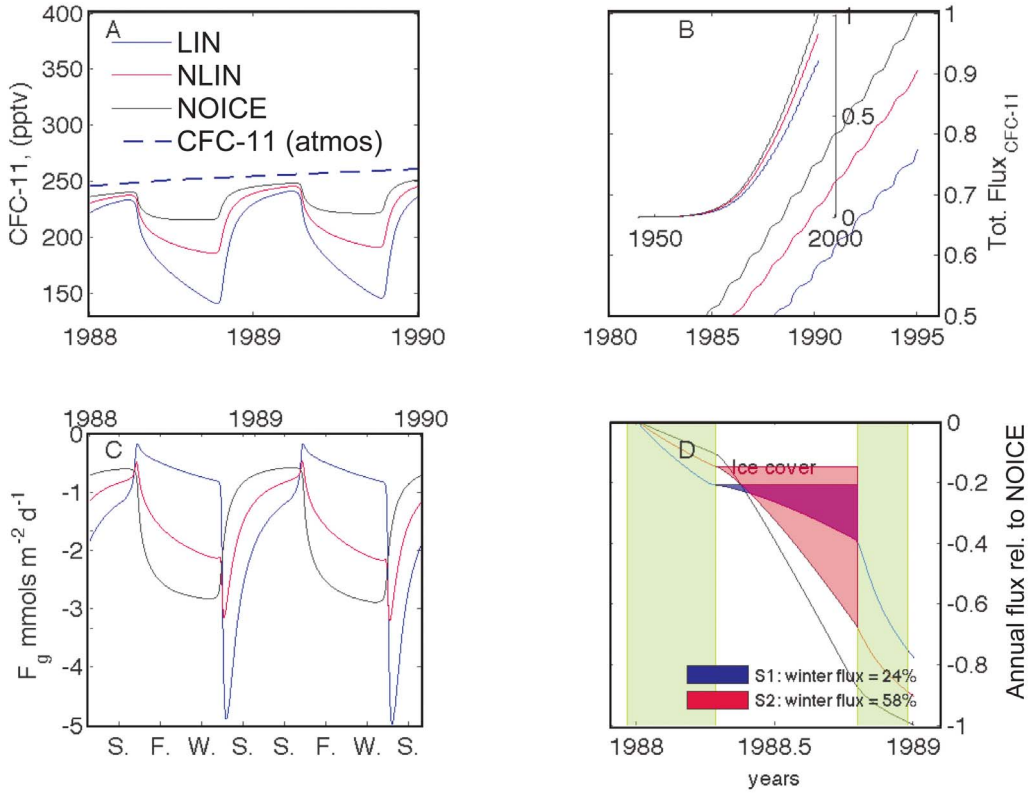

Figure 10. Results from OSL model uptake of CFC-11. (a) The surface ocean concentration for LIN, NLIN, and NOICE in comparison with the atmospheric time history (dashed line). (b) The time series of total CFC flux for the three scenarios, relative to the NOICE control scenario, which produced the greatest flux. (c) The variation in surface flux is indicated by season and (d) the integrated flux over a single year. The filled wedges indicate the amount of flux through the ice cover for LIN and NLIN, and the legend indicates the percent of annual flux that occurs under ice cover.

reduction in F_g for scenario NOICE as stratification sets in. In contrast, both LIN and NLIN experience a spike in flux in spring. For a brief period of time, F_g increases for LIN by almost a factor of five during melt out (Figure 10c). Measured at the end of winter the yearly cumulative flux for LIN is 60% less than the cumulative flux for NOICE, but this difference closes to only 22% by the end of spring. On a year-by-year basis, the net CFC-11 uptake from the atmosphere to the ocean interior, was only 25% smaller for LIN than for NOICE, despite the nearly 50% reduction in k, from 2.7 to 1.3 m d^{-1}.

3.2. Deep Ocean CO_2 Escape Through the SIZ

[34] We have shown that sea ice restriction of gas exchange can have a measureable impact on CFC-11 uptake and that uptake through sea ice can be an important part of the annual uptake. How does the picture change for CO_2, with a much longer time scale for gas exchange? For CO_2 the gas flux is expressed in terms of the disequilibrium between the total dissolved inorganic carbon (DIC) and the DIC in equilibrium with the atmosphere (DIC_{atm_eq}):

$$F_g = k_{CO_2}\alpha_0\beta\left(DIC_{atm\_eq} - DIC\right) \tag{13}$$

[35] The ionization fraction, α_0, and the buffer factor, β, define the equilibration of atmospheric CO_2 with carbonic acid across the air-sea interface, and the equilibrium distribution between carbonic acid, bicarbonate and carbonate [*Follows and Williams*, 2004]

$$\alpha_0 = \frac{H\mathrm{pCO}_2^{\mathrm{atm}}}{DIC_{atm\_eq}}, \quad \beta^{t+1} = \frac{\mathrm{pCO}_2^{\mathrm{atm}} - \mathrm{pCO}_2^{\mathrm{t}}}{\mathrm{pCO}_2^{\mathrm{atm}}}\frac{DIC_{atm\_eq}}{DIC_{atm\_eq} - DIC^t} \tag{14}$$

β depends on the instantaneous surface ocean DIC^t and pCO_2^t values and therefore varies in time. Under the assumption of constant temperature and salinity conditions, α_0 will remain constant. At salinity of 34 psu and T = 0°C, the term $\alpha_0\beta$ is approximately 0.13. The annual averages of k_{CO2}, during LIN, NLIN and NOICE are 1.7, 2.2 and 3.4 m d^{-1}, respectively, approximately 23% larger than $k_{CFC\text{-}11}$, and this is because CO_2 is lighter than CFC-11 and has a greater molecular diffusivity in water, which is reflected in the Schmidt number.

[36] The scenarios for transport of deep ocean "natural" CO_2 follow the same conditions as those for CFC-11. However, the air-sea flux of natural carbon through the Southern Ocean is directly related to surface ocean pCO_2, which in turn is partly controlled by biology. Therefore,

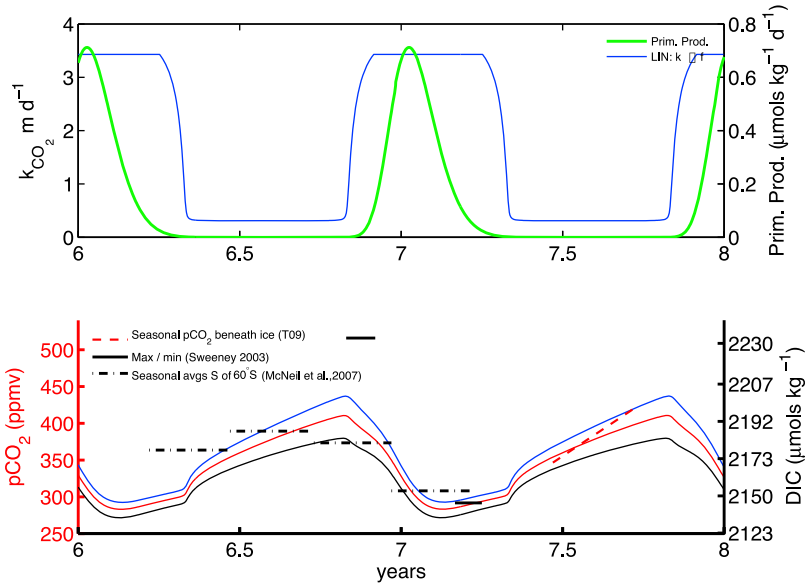

Figure 11. (top) k_{CO2} and primary productivity in comparison with (bottom) the surface ocean pCO_2 and DIC over a 2 year segment of the simulation. The simulation uses a constant atmospheric pCO_2 = 278 ppmv to represent a steady state atmospheric forcing condition. For reference, the linear trend of increasing pCO_2 beneath ice from T09 (pCO_2 = 0.802 * days + 208.9) is plotted as a dashed line. The seasonal averages of all DIC data south of 60°S comes from the gridded data set of *McNeil et al.* [2007], and the maximum and minimum of DIC of *Sweeney* [2003] is plotted as a solid line segment.

the simulations for CO_2 use "abiotic" and "biotic" cases. For the biotic case, a CO_2 sink is added to the right side of equation (8). The primary production bloom is represented by a Weibull distribution and is constructed so that primary production is at a maximum during a 2 month period, and the discrete time integral over a 1 year period is equal to the average rate of net CO_2 consumption estimated to be 57 g m^{-2} yr^{-1} by *Arrigo et al.* [2008a] When this value is spread over the top 50 m of the water column, it can be expressed as 94.9 μmols L^{-1} yr^{-1}. The fluctuation is exactly in phase with the seasonal variations in k. The effect is to produce a biological drawdown in pCO_2, which is timed to be directly out of phase with the advance and retreat of the seasonal sea ice cover (Figure 11).

[37] Equation (8) is solved for the time and depth-varying DIC^t concentration in μmol kg^{-1}, and then pCO_2 is determined using DIC^t and the dissociation constants for seawater [*Zeebe and Wolf-Gladrow*, 2001], assuming that the alkalinity in the OSL remains constant at 2300 μmol kg^{-1}. The ambient forcing is meant to illustrate the control of inorganic carbon flux in the seasonal ice zone. For simplicity, the time invariant preindustrial atmospheric concentration of CO_2 is set to 278 ppmv [*Ito et al.*, 2004], which in turn is used, along with alkalinity, to define DIC_{atm_eq} = 2134 μmol kg^{-1} by solving the carbonate equilibrium equations. The lower boundary is maintained at a constant DIC of 2250 μmol kg^{-1}, based on the aqueous concentration observed along S4I (Figure 7).

3.3. Biotic Versus Abiotic Scenarios

[38] The biotic seasonal cycle in surface ocean pCO_2/DIC fluctuates between 291/2145 and 437/2203 ppmv/μmol kg^{-1} for scenario LIN and between 284/2141 and 416/2196 ppmv/μmol kg^{-1} for scenario NLIN (Figure 11). In comparison, T09 estimated a late winter mean pCO_2 of 420 ppmv for the seasonal ice zone. The range of model fluctuations between all three scenarios is within the extrema from the seasonal carbonate system climatology by *McNeil et al.* [2007], which ranged between a summer minimum in DIC of 2075 μmol kg^{-1} and a winter maximum of 2239 μmol kg^{-1}. The seasonal averages of DIC from the *McNeil et al.* [2007] gridded data set have been plotted in Figure 11, and these depict a more muted oscillation in comparison to the model results. Finally, the maximum and minimum in the DIC cycle from the Ross Sea [*Sweeney*, 2003] show a minimum similar to that produced by the OSL model, but a maximum of 2233 μmol kg^{-1}, which is 21 μmol kg^{-1} higher than the winter maximum for scenario LIN. Examining each scenario for surface ocean pCO_2/DIC (Figure 11) it is apparent that LIN intersects the available field measurements of pCO_2 from *Sweeney* [2003] and *McNeil et al.* [2007] and T09 a total of four times, NLIN intersects this set of measurements five times and NOICE intersects them two times. On the basis of this semiquantitative criteria, NLIN would appear to be the scenario that most closely resembles the field data from the Southern Ocean.

[39] The most noticeable difference between the biotic and abiotic simulations is a reduction in the DIC concentration throughout the year, both in the surface layer and throughout the water column above 200 m (Figure 12). The reduction in DIC amounts to approximately 22 μmol kg^{-1} in summer and approximately 19 μmol kg^{-1} in winter. The persistence of the biotic depletion of DIC into winter indicates that gas exchange together with CDW renewal from beneath are not sufficient to completely erase the effect of summer primary production and restore the concentration to the abiotic winter state. One symptom of the reduced surface ocean DIC concentration is a reduction in the net CO_2 flux

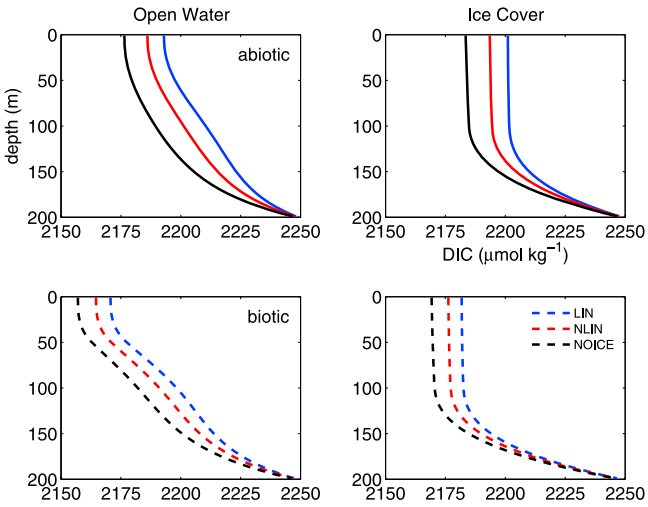

Figure 12. Vertical profiles of dissolved inorganic carbon (DIC) in the ocean surface layer (OSL) model, under abiotic (solid lines) and biotic (dashed lines) scenarios with open water and with ice cover.

(F_{CO2}) in both winter and summer: F_{CO2} is 35% less in winter and 47% less in summer as a result of photosynthesis in the surface layer in scenario LIN. F_{CO2} is 39% less in summer and 51% less in winter for scenario NLIN.

3.4. Sea Ice Impedance of CO_2 Flux

[40] In section 3.3 we reviewed similarities and differences between the biotic and abiotic DIC transport scenarios, in this section we focus on the biotic simulation and discuss the effect of sea ice on seasonal and annual CO_2 fluxes (F_{CO2}). The annual cycle of F_{CO2} is similar to that of the flux of CFC-11 in several respects. In particular, the net of F_{CO2} during ice cover is a significant portion of the net flux for the year, 46% for NLIN and 14% for LIN (Figure 13), which is less than the totals for CFC-11 (58% and 24%, respectively). Whereas both CO_2 and CFC-11 experience strong air-sea gradients in winter, the CO_2 flux time scale is reduced as a result of the equilibration factors, α_0 and β [*Haine*, 2006]. Although k_{CO2} is 30% larger than k_{CFC-11}, $k_{CO2}\alpha_0\beta = 0.48$ m d^{-1}, i.e., 80% less than k_{CFC-11}, and this is apparent in the reduced winter flux of CO_2 compared to CFC-11.

[41] A strong peak in F_{CO2} accompanies the springtime retreat of the ice cover (Figure 14). F_{CO2} in spring increases ninefold in LIN and twofold in NLIN, during a coincident period, while the flux in NOICE decreases as a result of stratification and in the absence of a strong ice-induced air-sea difference in CO_2 concentration. At the end of winter, the cumulative annual flux for LIN is 53% less than NOICE, but this difference closes to 41% by the end of spring (Figure 13). This result highlights the importance of the physical processes that take place in the marginal ice zone – the region of the seasonal ice zone that was ice covered in the past 30 d.

[42] The net annual flux of carbon in the biotic scenario is 2.3, 2.8 and 3.9 mol m^{-2} yr^{-1} for LIN, NLIN and NOICE, respectively (Table 1). Just as for CFC-11 the reductions in net flux of CO_2 between the LIN and NLIN scenarios and the NOICE scenario are smaller than the differences in mean annual k_{CO2} between LIN, NLIN and NOICE, e.g., k_{CO2} of LIN is 51% of k_{CO2} in NOICE. The smaller reduction in the values of F_{CO2} as compared to the values of k_{CO2} can be explained by rapid gas flux that occurs as the ice cover retreats in spring to expose a gas-rich water column. That is, the tighter restriction on gas exchange (i.e., LIN) leads to larger air-sea concentration gradient at the end of winter and a larger flux as the ice cover retreats. For LIN, F_{CO2} in the first 90 d after ice cover retreat represents 68% of the net annual flux (Figure 14), while the same period represents only 48% of the F_{CO2} for NLIN. This large flux occurs despite the coincident peak in primary productivity that is timed with the sea ice cover retreat. This result contrasts with the seasonal rectification hypothesis proposed by *Yager et al.* [1995], indicating that primary production during spring was insufficient to consume the excess in DIC left from winter ice cover. However, neither this simulation nor the studies cited in section 1 that indicate seasonal rectification of CO_2 can conclusively resolve the net effect of ice cover and photosynthesis, because realistic constraints on upwelling and gas exchange are not available.

3.5. Phasing Between Sea Ice and Spring Bloom

[43] The identification of a strong sea to air CO_2 flux despite photosynthesis raises a related question concerning the importance of the timing of the spring phytoplankton bloom in relation to the retreat of ice cover (Figure 14). To explore the importance of timing we changed the phase lag in the idealized primary productivity curve. By shifting the peak to occur 45 d earlier (−45) and 45 d later (+45), we obtain a qualitative sense of spring CO_2 efflux shifts by photosynthesis. Figure 15a shows the change in the primary production curve that results from these phase shifts. The +45 scenario reduces the magnitude of the peak springtime F_{CO2} by 4% and high CO_2 efflux is maintained for a longer

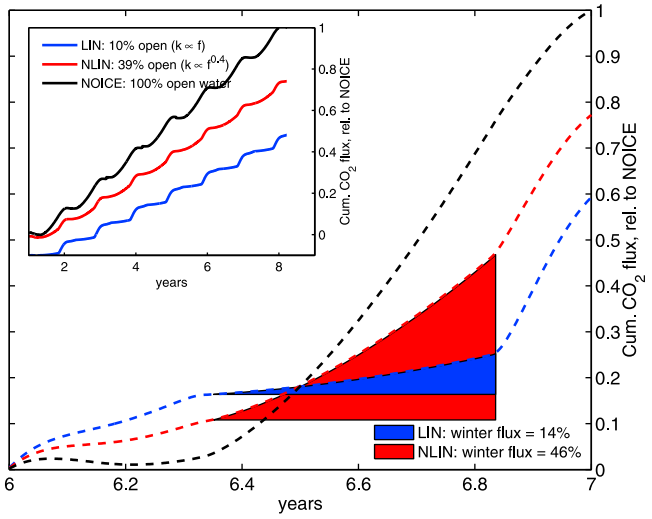

Figure 13. The cumulative net annual and net multiyear (inset) CO_2 flux from the ocean surface layer model in the "biotic scenario." The cumulative fluxes relative to the control scenario (NOICE) with no modulation of gas exchange by sea ice cover. The filled wedges indicate the net flux during ice-covered conditions and the legend lists the percentage of the annual flux that took place during the ice-covered period.

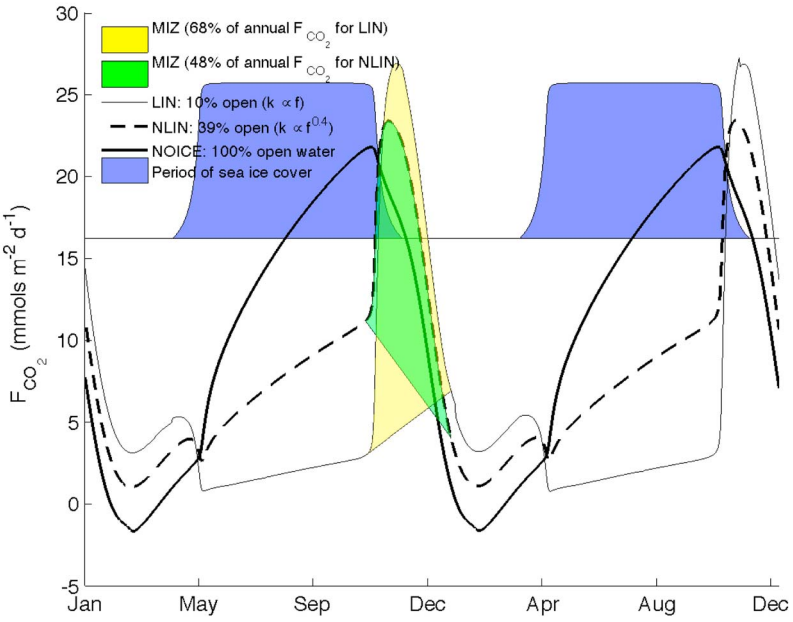

Figure 14. The seasonal cycle in the instantaneous CO_2 flux, F_{CO2}, over a 2 year period, depicting the timing of the maxima and minima in F_{CO2} in relationship to the sea ice cycle in the transport model. The shaded areas underneath the LIN and NLIN curves indicate the area under these curves for the first 90 d immediately following ice cover retreat. For LIN this area represents 68% of the net annual sum of F_{CO2}.

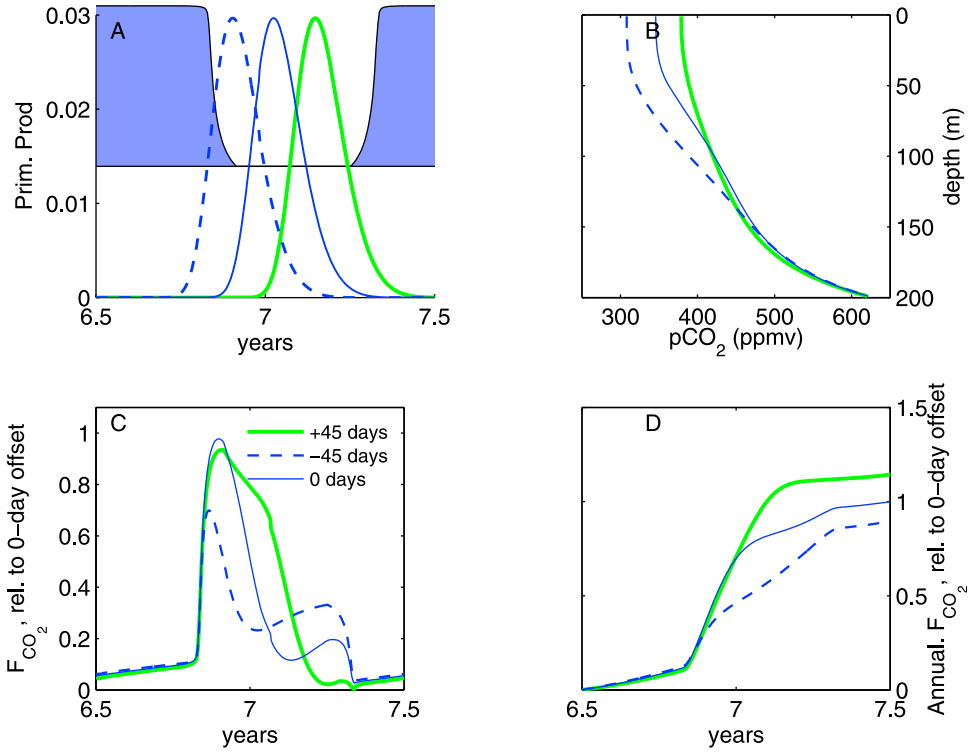

Figure 15. Differences in CO_2 flux when primary production is offset to occur −45, 0, and +45 d out-of-phase from the seasonal ice cover cycle. (a) The phase shift in the forcing, (b) the difference in the vertical profiles during ice cover, (c) the instantaneous flux over a 1 year period, and (d) the cumulative sum of F_{CO2} over 1 year.

time during the ice-free period, compared to the scenario with no phase shift. A shift by −45 also produces a decrease in the maximum F_{CO2}, by 27% compared to the no phase shift case. This decrease in maximum F_{CO2} is partially offset by a larger flux at the end of the ice-free period as stratification is eroded (near 7.25 years, Figure 15c). When viewing the cumulative annual F_{CO2}, there is a consistent trend in the annual flux: For the +45 d scenario, annual F_{CO2} is 114% of the 0 d shift and for the −45 scenario it is 89% of the no shift case. The later the primary production bloom occurs, the larger the net annual flux of CO_2 from the SIZ. This exercise helps to probe the relationship between sea ice cover and primary production, however it should be noted that there is little evidence for large variations in the timing between sea ice melt and the spring bloom – most studies demonstrate a tight coupling between the two processes [*Sukhanova et al.*, 2009; *Tortell and Long*, 2009], with the phytoplankton bloom occurring some two weeks after ice breakup [*Dünweber et al.*, 2010].

4. Summary and Conclusions

[44] This study has explored gas exchange in the presence of sea ice, with focus on the gas transfer velocity, k, and its parameterization in the sea ice zone. There are very few data-based estimates of k from the sea ice zone that can be used to constrain gas exchange rates in these settings. The results from the tracer mass balance in this study relate to nearly 100% sea ice cover, with an average value of 0.11 m d^{-1} at 95% confidence, indicating a small but detectable gas exchange for nearly complete sea ice cover conditions. In contrast, *Fanning and Torres* [1991] presented the only other available estimates of k under partial sea ice cover. Their results yield a minimum of k_{660} = 1.4 m d^{-1} under approximately 90% sea ice cover conditions, and this value is approximately three times greater than that expected from a linear scaling between gas exchange and open water. Collectively, these results serve to demonstrate the paucity of information that can be used to constrain k in sea ice covered regions. Furthermore, the conditions that lead to relatively large values of k [*Fanning and Torres*, 1991] under relatively restrictive sea ice cover may be caused by turbulence production mechanisms other than wind. Turbulence in the sea ice zone can arise in the ice water boundary layer as a result of current shear and buoyant convection [*McPhee*, 1992; *Morison et al.*, 1992]. These processes imply that fetch reduction by sea ice cover is not a sufficient constraint to determine the air-sea gas exchange through the sea ice pack.

[45] The results of the ocean surface layer model emphasize the importance of establishing the rate of gas ventilation during all conditions of sea ice cover. The flux of CO_2 through the winter ice cover represents between 14% and 46% of the net annual CO_2 flux, depending on the parameterization between sea ice cover and k that is used. A further surprising result of these simulations is the observation that tighter restriction of CO_2 in winter results in larger CO_2 flux in spring as the sea ice cover retreats. This indicates that sea ice cover may serve only to delay the CO_2 flux until spring. This result differs from the CO_2 rectification (by primary production) hypothesis proposed by *Yager et al.* [1995] and investigated by *Sweeney* [2003] and others. To adequately determine the net effect of gas exchange and primary production will require process studies in the marginal ice zone to determine both physical and biological gasdynamics in this complex and dynamic region. Spring bloom in the marginal ice zone takes place in a stratified water column surrounded by sea ice floes, brash and potentially new frazil or pancake ice. To parameterize the biogenic gas fluxes during this period it will be necessary to establish and prioritize the turbulent forcing mechanisms as well as the strength and timing of the phytoplankton bloom, in relation to the retreat of the ice edge in spring.

[46] **Acknowledgments.** We would like to thank Bill Smethie, the LDEO Cluorofluorocabon Lab and Bruce Huber for providing CFC and hydrographic data from Ice Station Weddell. We gratefully acknowledge the insightful comments and suggestions of Rik Wanninkhof and two anonymous reviewers. Support for this work was provided by the Climate Center at the Lamont-Doherty Earth Observatory, an NSF IGERT Fellowship and a NOAA Climate and Global Change Postdoctoral Fellowship to BL, and NSF grant OPP 01-25523/ANT 04-40825 (PS). LDEO contribution 7494.

References

Arrigo, K. R., and G. L. Van Dijken (2007), Interannual variation in air-sea CO_2 flux in the Ross Sea, Antarctica: A model analysis, *J. Geophys. Res.*, *112*, C03020, doi:10.1029/2006JC003492.

Arrigo, K. R., G. L. van Dijken, and S. Bushinsky (2008a), Primary production in the Southern Ocean 1997–2006, *J. Geophys. Res.*, *113*, C08004, doi:10.1029/2007JC004551.

Arrigo, K. R., G. L. van Dijken, and S. Pabi (2008b), Impact of a shrinking Arctic ice cover on marine primary production, *Geophys. Res. Lett.*, *35*, L19603, doi:10.1029/2008GL035028.

Bakker, D. C. E., H. J. W. DeBaar, and U. V. Bathmann (1997), Changes of carbon dioxide in surface waters during spring in the Southern Ocean, *Deep Sea Res., Part II*, *44*, 91–127, doi:10.1016/S0967-0645(96)00075-6.

Cavalieri, D., C. Parkinson, P. Gloerson, and H. J. Zwally (1996), Sea ice concentrations from Nimbus-7 SMMR and DMSP SSM/I passive microwave data, digital media, Natl. Snow and Ice Data Cent., Boulder, Colo.

Comiso, J. C. (2007), Bootstrap sea ice concentrations from Nimbus-7 SMMR and DMSP SSM/I, digital media, Natl. Snow and Ice Data Cent., Boulder, Colo.

Cox, G. F. N., and W. F. Weeks (1983), Equations for determining the gas and brine volumes in sea-ice samples, *J. Glaciol.*, *29*, 306–316.

Dünweber, M., R. Swalethorp, S. Kjellerup, T. G. Nielsen, K. E. Arendt, and M. Hjorth (2010), Succession and fate of the spring diatom bloom in Disko Bay, western Greenland, *Mar. Ecol. Prog. Ser.*, *419*, 11–29, doi:10.3354/meps08813.

Fanning, K. A., and L. M. Torres (1991), ^{222}Rn and ^{226}Ra: Indicators of sea-ice effects on air-sea gas exchange, *Polar Res.*, *10*, 51–58, doi:10.1111/j.1751-8369.1991.tb00634.x.

Follows, M., and R. G. Williams (2004), Air-sea flux of CO_2 in the North Atlantic, in *The Ocean Carbon Cycle and Climate*, edited by M. Follows and T. Oguz, pp. 217–249, Kluwer Acad., Dordrecht, Netherlands.

Geiger, C. A., and M. R. Drinkwater (2005), Coincident buoy- and SAR-derived surface fluxes in the western Weddell Sea during Ice Station Weddell 1992, *J. Geophys. Res.*, *110*, C04002, doi:10.1029/2003JC002112.

Gibson, J. A. E., and T. W. Trull (1999), Annual cycle of fCO_2 under sea-ice and in open water in Prydz Bay, East Antarctica, *Mar. Chem.*, *66*, 187–200, doi:10.1016/S0304-4203(99)00040-7.

Haine, T. W. N. (2006), On tracer boundary conditions for geophysical reservoirs: How to find the boundary concentration from a mixed condition, *J. Geophys. Res.*, *111*, C05003, doi:10.1029/2005JC003215.

Hohmann, R., P. Schlosser, and B. Huber (2003), Helium 3 and dissolved oxygen balances in the upper waters of the Weddell Sea: Implications for oceanic heat fluxes, *J. Geophys. Res.*, *108*(C3), 3087, doi:10.1029/2000JC000474.

Huber, B., P. A. Mele, W. E. Haines, A. L. Gordon, and V. I. Lukin (1994), 1 CTD/Hydrography Data, *Tech. Rep. LDEO 94-2*, Lamont-Doherty Earth Obs., Palisades, N. Y.

Ito, T., J. Marshall, and M. Follows (2004), What controls the uptake of transient tracers in the Southern Ocean?, *Global Biogeochem. Cycles*, *18*, GB2021, doi:10.1029/2003GB002103.

Jones, E., D. C. E. Bakker, H. J. Venables, M. J. Whitehouse, R. E. Korb, and A. J. Watson (2010), Rapid changes in surface water carbonate

chemistry during Antarctic sea ice melt, *Tellus, Ser. B*, *62*, 621–635, doi:10.1111/j.1600-0889.2010.00496.x.

Knuth, M., and S. F. Ackley (2006), Summer and early fall sea-ice concentration in the Ross Sea: Comparison of in situ ASPeCt observations and satellite passive microwave estimates, *Ann. Glaciol.*, *44*, 303–309, doi:10.3189/172756406781811466.

Le Quéré, C., et al. (2007), Saturation of the Southern Ocean CO_2 sink due to recent climate change, *Science*, *316*, 1735–1738, doi:10.1126/science.1136188.

Lindsay, R. W., and D. A. Rothrock (1995), Arctic sea ice leads from advanced very high resolution radiometer images, *J. Geophys. Res.*, *100*, 4533–4544, doi:10.1029/94JC02393.

Loose, B., W. R. McGillis, P. Schlosser, D. Perovich, and T. Takahashi (2009), The effects of freezing, growth and ice cover on gas transport processes in laboratory seawater experiments, *Geophys. Res. Lett.*, *36*, L05603, doi:10.1029/2008GL036318.

Lovenduski, N., N. Gruber, and S. Doney (2008), Toward a mechanistic understanding of the decadal trends in the Southern Ocean carbon sink, *Global Biogeochem. Cycles*, *22*, GB3016, doi:10.1029/2007GB003139.

Lytle, V. I., and S. F. Ackley (1996), Heat flux through sea ice in the western Weddell Sea: Convective and conductive transfer processes, *J. Geophys. Res.*, *101*, 8853–8868, doi:10.1029/95JC03675.

Marinov, I., A. Gnanadesikan, J. R. Toggweiler, and J. L. Sarmiento (2006), The Southern Ocean biogeochemical divide, *Nature*, *441*, 964–967, doi:10.1038/nature04883.

McNeil, B. I., N. Metzl, R. M. Key, R. J. Matear, and A. Corbiere (2007), An empirical estimate of the Southern Ocean air-sea CO_2 flux, *Global Biogeochem. Cycles*, *21*, GB3011, doi:10.1029/2007GB002991.

McPhee, M. (1992), Turbulent heat flux in the upper ocean under sea ice, *J. Geophys. Res.*, *97*, 5365–5379, doi:10.1029/92JC00239.

McPhee, M., and D. G. Martinson (1994), Turbulent mixing under drifting pack ice in the Weddell Sea, *Science*, *263*, 218–221, doi:10.1126/science.263.5144.218.

Meier, W., F. Fetterer, K. Knowles, M. Savoie, and M. J. Brodzik (2006), Sea ice concentrations from Nimbus 7 SMMR and DMSP SSM/I passive microwave data, 1978–2009, digital media, Natl. Snow and Ice Data Cent., Boulder, Colo.

Morison, J. H., M. McPhee, T. B. Curtin, and T. B. Paulson (1992), The oceanography of winter leads, *J. Geophys. Res.*, *97*, 11,199–11,218, doi:10.1029/92JC00684.

Ou, H. W. (1991), Some effects of a seamount on oceanic flows, *J. Phys. Oceanogr.*, *21*, 1835–1845, doi:10.1175/1520-0485(1991)021<1835:SEOASO>2.0.CO;2.

Sarmiento, J. L., J. C. Orr, and U. Siegenthaler (1992), A perturbation simulation of uptake in an ocean general circulation model, *J. Geophys. Res.*, *97*, 3621–3645, doi:10.1029/91JC02849.

Schlosser, P., W. Roether, and G. Rohardt (1987), Helium-3 balance of the upper layers of the northwestern Weddell sea, *Deep Sea Res., Part A*, *34*, 365–377, doi:10.1016/0198-0149(87)90143-9.

Shashkov, M., and S. Steinberg (1996), Solving diffusion equations with rough coefficients in rough grids, *J. Comput. Phys.*, *129*, 383–405, doi:10.1006/jcph.1996.0257.

Steffen, K., and A. Schweiger (1991), NASA team algorithm for sea ice concentration retrieval from Defense Meteorological Satellite Program special sensor microwave imager: Comparison with Landsat satellite imagery, *J. Geophys. Res.*, *96*, 21,971–21,987, doi:10.1029/91JC02334.

Sukhanova, I. N., M. V. Flint, L. A. Pautova, D. A. Stockwell, J. M. Grebmeier, and V. M. Sergeeva (2009), Phytoplankton of the western Arctic in the spring and summer of 2002: Structure and seasonal changes, *Deep Sea Res., Part II*, *56*, 1223–1236, doi:10.1016/j.dsr2.2008.12.030.

Sweeney, C. (2003), The annual cycle of surface CO_2 and O_2 in the Ross Sea: A model for gas exchange on the continental shelves of Antarctica, in *Biogeochemistry of the Ross Sea*, *Antarct. Res. Ser.*, vol. 78, edited by G. R. DiTullio and R. B. Dunbar, pp. 295–312, AGU, Washington, D. C.

Takahashi, T., R. H. Wanninkhof, D. W. Chipman, S. C. Sutherland, and T. T. Takahashi (1997), Global air-sea flux of CO_2: An estimate based on measurements of sea-air pCO_2 difference, *Proc. Natl. Acad. Sci. U. S. A.*, *94*, 8292–8299, doi:10.1073/pnas.94.16.8292.

Takahashi, T., et al. (2002), Global sea-air CO_2 flux based on climatological surface ocean pCO_2, and seasonal biological and temperature effects, *Deep Sea Res., Part II*, *49*, 1601–1622, doi:10.1016/S0967-0645(02)00003-6.

Takahashi, T., et al. (2009), Climatological mean and decadal change in surface ocean pCO_2, and net sea-air CO_2 flux over the global oceans, *Deep Sea Res., Part II*, *56*, 554–577, doi:10.1016/j.dsr2.2008.12.009.

Tarantola, A. (2005), *Inverse Problem Theory and Methods for Model Parameter Estimation*, Soc. for Ind. and Appl. Math., Philadelphia, Pa., doi:10.1137/1.9780898717921.

Tortell, P. D., and M. C. Long (2009), Spatial and temporal variability of biogenic gases during the Southern Ocean spring bloom, *Geophys. Res. Lett.*, *36*, L01603, doi:10.1029/2008GL035819.

Walker, S. J., R. F. Weiss, and P. K. Salameh (2000), Reconstructed histories of the annual mean atmospheric mole fractions for the halocarbons CFC-11, CFC-12, CFC-113, and carbon tetrachloride, *J. Geophys. Res.*, *105*, 14,285–14,296, doi:10.1029/1999JC900273.

Yager, P. L., D. W. R. Wallace, K. Johnson, W. O. Smith, P. J. Minnett, and J. W. Deming (1995), The Northeast Water Polynya as an atmospheric CO_2 sink: A seasonal rectification hypothesis, *J. Geophys. Res.*, *100*, 4389–4398, doi:10.1029/94JC01962.

Zeebe, R. E., and D. Wolf-Gladrow (2001), *CO_2 in Seawater: Equilibrium, Kinetics, Isotopes*, *Elsevier Oceanogr. Ser.*, vol. 65, Elsevier, New York.

B. Loose, Department of Marine Chemistry and Geochemistry, Woods Hole Oceanographic Institution, Woods Hole, MA 02543, USA. (brice@whoi.edu)

P. Schlosser, Lamont-Doherty Earth Observatory, Earth Institute at Columbia University, 61 Rte. 9W, Palisades, NY 10964, USA.